

Ultrafast hot-hole injection modifies hot-electron dynamics in Au/p-GaN heterostructures

Giulia Tagliabue ^{ID}^{1,2,12}, Joseph S. DuChene^{1,2,12}, Mohamed Abdellah^{3,4,12}, Adela Habib⁵, David J. Gosztola ^{ID}⁶, Yocef Hattori³, Wen-Hui Cheng ^{ID}^{1,2}, Kaibo Zheng^{7,8}, Sophie E. Canton ^{ID}^{9,10}, Ravishankar Sundararaman⁵, Jacinto Sá ^{ID}^{3,11} and Harry A. Atwater ^{ID}^{1,2}

A fundamental understanding of hot-carrier dynamics in photo-excited metal nanostructures is needed to unlock their potential for photodetection and photocatalysis. Despite numerous studies on the ultrafast dynamics of hot electrons, so far, the temporal evolution of hot holes in metal–semiconductor heterostructures remains unknown. Here, we report ultrafast ($t < 200$ fs) hot-hole injection from Au nanoparticles into the valence band of p-type GaN. The removal of hot holes from below the Au Fermi level is observed to substantially alter the thermalization dynamics of hot electrons, reducing the peak electronic temperature and the electron–phonon coupling time of the Au nanoparticles. First-principles calculations reveal that hot-hole injection modifies the relaxation dynamics of hot electrons in Au nanoparticles by modulating the electronic structure of the metal on timescales commensurate with electron–electron scattering. These results advance our understanding of hot-hole dynamics in metal–semiconductor heterostructures and offer additional strategies for manipulating the dynamics of hot carriers on ultrafast timescales.

The absorption of light by metallic nanostructures generates a non-equilibrium distribution of hot electrons and hot holes in the metal (Fig. 1). Collecting these hot carriers on ultrafast timescales holds great promise for non-equilibrium optoelectronics and photocatalysis^{1–13}, but to do so effectively requires a complete understanding of the ensuing carrier dynamics that occur after light absorption. Numerous spectroscopic studies^{14–20} have led to the following picture of ultrafast hot-carrier dynamics in metals. Upon photo-excitation, the initial energy distribution of hot carriers above and below the metal Fermi level is collectively controlled by both the incident photon energy and the metal band structure^{9,27–29}. These non-thermal hot carriers then quickly equilibrate via electron–electron scattering processes on an ultrafast timescale ($t \approx$ fs–ps) to establish a distribution with an elevated electronic temperature (T_e) relative to the temperature of the metallic lattice (T_l)^{14,15,20}. This excited hot-carrier distribution subsequently equilibrates with the underlying lattice via electron–phonon coupling ($t \approx$ ps–ns) as the nanostructure dissipates heat to its local surroundings ($t >$ ns)^{14,15,20}. Despite many studies of hot-carrier dynamics in metals, nearly all reports involve isolated colloidal nanoparticles. The realization of hot-carrier optoelectronics, however, requires interfacing metal nanostructures with semiconductors to facilitate carrier injection and transport within a device architecture^{1–3}. Indeed, the collection of hot carriers is typically accomplished through the formation of an interfacial Schottky junction with n-type (p-type) semiconductors^{1–11} to quickly capture hot electrons (hot holes) before their thermalization with the phonon bath ($t \approx$ 1 ps) (Fig. 1b,c). While the vast majority of metal–semiconductor heterostructures have

been devised to enable hot-electron collection^{1–11}, few systems suitable for hot-hole capture and conversion have been reported^{30,31}. Recent ab initio calculations indicate that the ultrafast dynamics of photo-excited hot electrons in metal nanostructures are highly sensitive to the electronic structure of the metal²⁹. Manipulating the d-band occupancy via ultrafast hot-hole injection to the valence band of a p-type semiconductor may offer additional opportunities for controlling the relaxation dynamics and shaping the energy distributions of hot carriers in metal nanostructures. To date, however, the ultrafast dynamics of hot holes in metal–semiconductor heterostructures remain unknown. An improved understanding of the carrier dynamics in hot-hole-driven systems is therefore needed to expand our knowledge of hot-carrier optoelectronics beyond hot electrons.

Our experimental platform for ultrafast studies of hot-carrier dynamics consists of gold (Au) nanoparticles dispersed onto p-type gallium nitride (p-GaN) substrates (Supplementary Fig. 1). We have previously demonstrated that Au/p-GaN heterostructures exhibit the ideal material properties to enable such experiments³⁰. The wide band gap of p-GaN ($E_g = 3.4$ eV) excludes visible-light excitation of free carriers directly within the semiconductor support, while also possessing the appropriate p-type character to facilitate the conduction of hot holes. A sizeable Schottky barrier ($\Phi_B = 1.1$ eV) is established across the Au/p-GaN interface, which ensures that only hot holes with energies in excess of 1.1 eV below the Au Fermi level can be injected into the valence band of the underlying p-GaN support³⁰. Our previous photoelectrochemical studies have also verified that only hot holes, and not hot electrons,

¹Thomas J. Watson Laboratory of Applied Physics, California Institute of Technology, Pasadena, CA, USA. ²Joint Center for Artificial Photosynthesis, California Institute of Technology, Pasadena, CA, USA. ³Department of Chemistry–Ångström Laboratory, Uppsala University, Uppsala, Sweden.

⁴Department of Chemistry, Qena Faculty of Science, South Valley University, Qena, Egypt. ⁵Department of Materials Science and Engineering, Rensselaer Polytechnic Institute, Troy, NY, USA. ⁶Center for Nanoscale Materials, Nanoscience and Technology Division, Argonne National Laboratory, Argonne, IL, USA. ⁷Department of Chemistry, Technical University of Denmark, Kongens Lyngby, Denmark. ⁸Department of Chemical Physics and NanoLund, Lund University, Lund, Sweden. ⁹ELI-ALPS, ELI-HU Non-Profit Ltd, Szeged, Hungary. ¹⁰Attoscience Group, Deutsche Elektronen Synchrotron (DESY), Hamburg, Germany. ¹¹Institute of Physical Chemistry, Polish Academy of Sciences, Warsaw, Poland. ¹²These authors contributed equally: Giulia Tagliabue, Joseph S. DuChene, Mohamed Abdellah. e-mail: jacinto.sa@kemi.uu.se; haa@caltech.edu

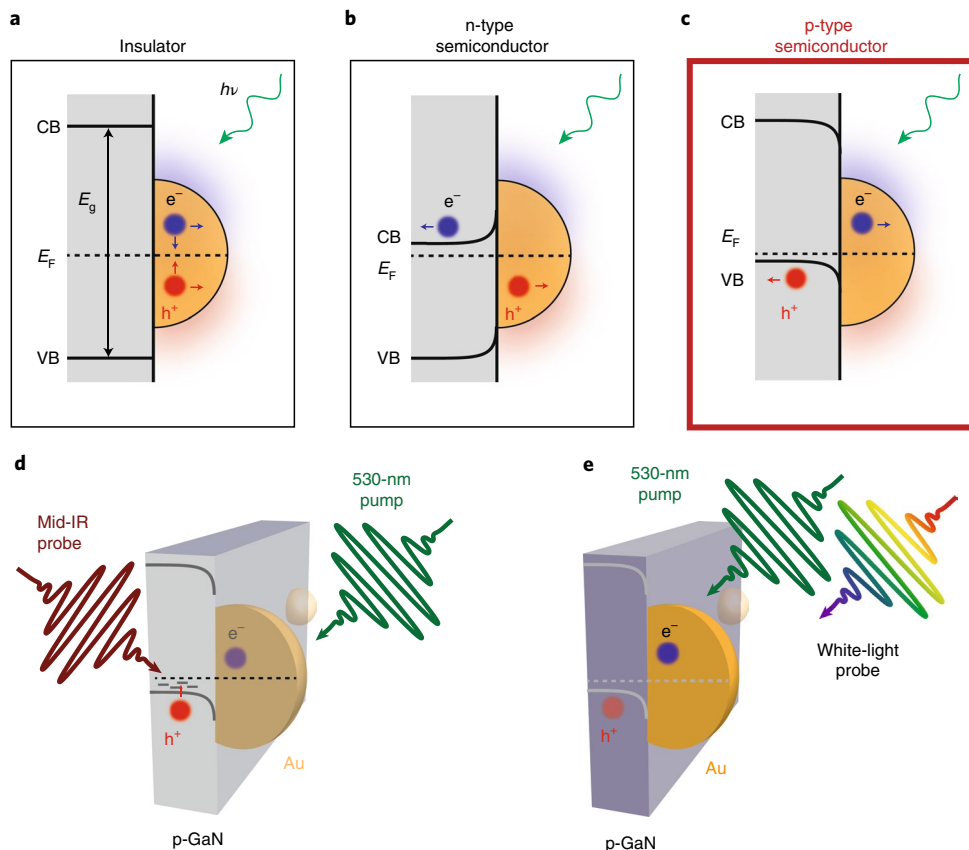


Fig. 1 | Optical excitation of hot carriers in metal nanostructures. **a–c**, Photogenerated hot electron–hole pair production in Au nanoparticles supported on an insulating substrate (**a**), an n-type semiconductor (**b**) or a p-type semiconductor (**c**) depicting the role of the substrate (grey) in preventing (**a**) or facilitating (**b,c**) interfacial charge separation of hot electron–hole (e–h) pairs (blue and red circles, respectively) at the metal–semiconductor heterojunction. The energies of the conduction band (CB, horizontal solid line), valence band (VB, horizontal solid line), band gap (E_g) and Fermi level (E_F , horizontal dashed line) are shown. In all cases, the incident photon energy ($h\nu$, green arrows) that excites hot carriers on the metal is less than E_g of the support. **d,e**, Experimental design for transient absorption pump–probe studies using a 530-nm pump wavelength to create hot electron–hole pairs on the Au nanoparticles and initiate hot-hole injection to the p-type GaN support while probing the dynamics of hot holes within the p-GaN valence band levels (horizontal solid lines) via infrared (IR) transient absorption spectroscopy (**d**), or probing the hot-electron dynamics on the Au nanoparticles across the visible regime with a broadband white-light probe (**e**).

are transferred to the p-GaN support upon optical excitation of the Au nanoparticles³⁰. These Au/p-GaN heterostructures therefore allow us to spectrally distinguish the dynamics of hot holes within the valence band of p-GaN, which can be probed in the infrared regime³² (Fig. 1d), from hot electrons in the metal, which are separately monitored across the visible spectrum with a broadband white-light probe^{14–18} (Fig. 1e).

Gold nanoparticles of diameter 7.3 ± 2.4 nm were uniformly deposited onto a p-type GaN epi-film on sapphire via electron-beam physical vapour deposition (Fig. 2a and Supplementary Fig. 1). The Au nanoparticles used for these studies were intentionally kept small to ensure that their physical dimensions remained commensurate with the very short, energy-dependent mean-free path (l_{mfp}) of hot holes in noble metals ($l_{\text{mfp}} \approx 5–10$ nm)^{27,28}. Only those carriers generated within a distance similar to the l_{mfp} from the interface are expected to contribute substantially to the injection process. No interfacial adhesion layer was used to construct the metal–semiconductor heterojunction (see Methods). The absorption spectrum of Au/p-GaN heterostructures exhibits a peak in the visible region at 568 nm, attributable to the surface plasmon resonance of Au nanoparticles (Fig. 2a, black curve). Fringes present in the spectra are due to Fabry–Pérot interference within the p-GaN epi-film (Fig. 2a, grey curve, and Supplementary Fig. 2).

Ultrafast dynamics of hot holes

The dynamics of photo-excited hot holes in Au/p-GaN heterostructures were monitored via ultrafast transient absorption spectroscopy (see Methods). Optical excitation of hot carriers in the Au nanoparticles was initiated with a 530-nm pump pulse (λ_{pump}) and the temporal evolution of hot holes injected into the p-GaN valence band was probed across the infrared regime (Fig. 1d and Extended Data Fig. 1). It has previously been shown that photo-excitation of Au nanoparticles at these pump energies ($h\nu = 2.34$ eV), above the interband threshold of the metal (~ 1.8 eV), preferentially produces hot holes within the Au d bands^{27,28,33}. As evidenced by the steep rise in transient absorption (ΔAbs) at a probe wavelength of $4.85\text{ }\mu\text{m}$, optical excitation induces hot-hole injection from Au nanoparticles into the p-GaN valence band within the 200-fs temporal resolution of our experimental setup (Fig. 2b, black squares). This observation confirms that hot-hole injection in Au/p-GaN heterostructures occurs on a similar timescale to that previously reported for hot-electron injection at the Au/TiO₂ interface^{22,23}.

The relaxation dynamics of hot holes can be fit to a multi-exponential function, which exhibits a fast decay component (τ_1) on the ~ 1 ps timescale commensurate with electron–phonon coupling in the p-GaN support³⁴, followed by two slower components; one occurs on the tens of picoseconds timescale

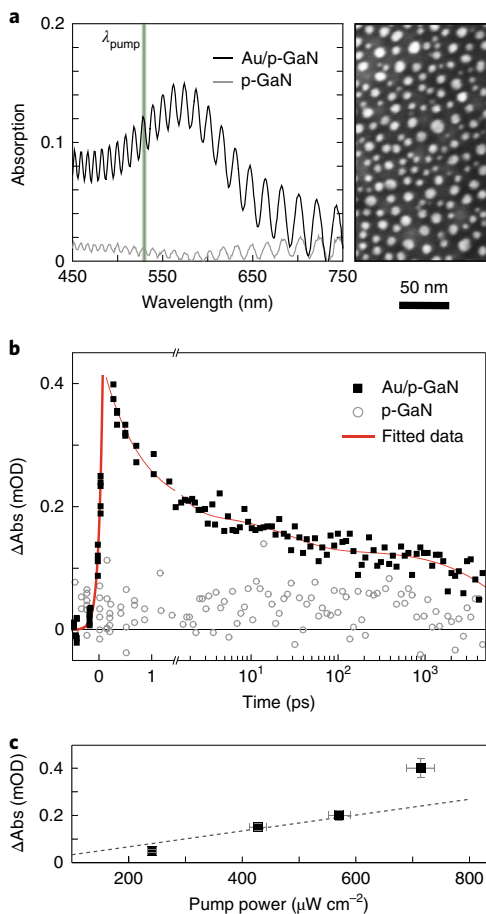


Fig. 2 | Infrared transient absorption spectroscopy of hot-hole dynamics in Au/p-GaN heterostructures. **a**, Absorption spectra of Au/p-GaN heterostructures (black curve) and bare p-GaN substrate (grey curve) along with the corresponding SEM image of Au nanoparticles (mean diameter, $d=7.3\pm2.4$ nm) on p-GaN support. The vertical green line indicates the pump laser wavelength, $\lambda_{\text{pump}}=530$ nm, used for optical excitation of the Au nanoparticles. **b**, Ultrafast transient rise and decay probed at $2,060\text{ cm}^{-1}$ ($\lambda_{\text{probe}}=4.85\mu\text{m}$) obtained from Au/p-GaN (black points) and bare p-GaN (open circles) upon 530-nm pump pulse at an incident power of 500 and $750\mu\text{W}$, respectively. The red line shows a fit to the experimental data, which exhibits an instrument-limited rise time of less than 200 fs. The horizontal grey line denotes the baseline $\Delta\text{Abs}=0$. **c**, Power-dependent transient absorption peak signal monitored at $2,060\text{ cm}^{-1}$ ($\lambda_{\text{probe}}=4.85\mu\text{m}$) from Au/p-GaN heterostructures displaying linear behaviour up to around $600\mu\text{W cm}^{-2}$. The error bars indicate the standard deviation about the mean and the dashed line serves as a guide to the eye.

($\tau_2 \approx 10$ ps) and another on the order of a few nanoseconds ($\tau_3 \approx 5$ ns). A distribution of charge-carrier traps and/or surface states may be responsible for the broad spread in observed relaxation times. We tentatively attribute the τ_2 component to trapping of hot holes within shallow traps located near the p-GaN valence band edge, and the τ_3 component to charge trapping within deep traps located within the p-GaN band gap. A linear relationship was observed between the incident pump power and the magnitude of the differential absorption signal (ΔAbs) from the Au/p-GaN sample at low incident power ($I_0 \leq 600\mu\text{W cm}^{-2}$) (Fig. 2c, black squares, and Extended Data Fig. 2). Two additional control experiments were performed to conclusively assign the origin of this transient absorption signal (ΔAbs) to hot-hole injection from Au to p-GaN. In the absence of Au nanoparticles, no transient absorption

response was observed from bare p-GaN substrates (Fig. 2b, open circles), confirming that the pump wavelength of 530 nm is incapable of exciting carriers directly within the p-GaN support. Similarly, excitation of Au nanoparticles supported on insulating ZrO_2 substrates, for which hot-carrier injection is prohibited²², fails to yield any spectroscopic signal (Extended Data Fig. 3). This result excludes the possibility that the signal observed in the mid-infrared with Au/p-GaN originates solely from photogenerated hot carriers that remain confined to the Au nanoparticles. Taken together, these observations demonstrate that optical excitation of the Au nanoparticles induces ultrafast ($t \leq 200$ fs) hot-hole injection to the p-GaN support.

Ultrafast dynamics of hot electrons

The electronic heat capacity ($C_e(T_e, N_e)$) of Au nanoparticles, which is proportional to both the electronic temperature (T_e) and the electron density (N_e), is highly sensitive to the electronic structure of the metal²⁹. Ultrafast hot-hole injection to the p-GaN valence band effectively raises N_e of the Au nanoparticles on timescales commensurate with electron-electron thermalization, thereby increasing $C_e(T_e, N_e)$ of the metal as the hot electrons are actively establishing an elevated T_e above the Au Fermi level. The electronic density of states and corresponding heat capacity $C_e(T_e, N_e)$ collectively determine the peak electronic temperature ($T_{e,\text{peak}}$) attained via electron-electron scattering processes²⁹. The observed ultrafast collection of hot holes is therefore anticipated to limit $T_{e,\text{peak}}$ of the electron gas and alter the subsequent thermalization dynamics of hot electrons left behind on the Au nanoparticles.

Since changes in the relaxation dynamics of the electron gas will be manifest in the electron–phonon coupling time ($\tau_{e-\text{ph}}$) of the Au nanoparticles^{14–18}, we employed ultrafast transient absorption spectroscopy to probe subtle changes in the electron dynamics occurring on the metal due to hot-hole injection at the Au/p-GaN interface (see Methods). As a reference for the hot-electron dynamics observed on Au/p-GaN, we also prepared Au nanoparticles on insulating sapphire (Al_2O_3) and glass (SiO_2) supports (Supplementary Figs. 2 and 3). Given that the dynamics are pump-power dependent^{15,16}, the electron–phonon coupling time ($\tau_{e-\text{ph}}$) of the Au nanoparticles on the different substrates was obtained by fitting the relaxation dynamics at various pump powers (Extended Data Figs. 4–6). Although $\tau_{e-\text{ph}}$ is known to be independent of size for metal nanoparticles within the range studied here ($d=7\text{--}15$ nm)^{14–18}, the observed thermalization dynamics at a given pump power are proportional to the electronic temperature of the electron gas of photo-excited metal nanoparticles²¹. To account for variations in photon absorption due to differences in Au nanoparticle size, substrate coverage and optical density between the samples, the determined values of $\tau_{e-\text{ph}}$ are plotted as a function of the absorbed energy density, U_{abs} (J m^{-3}) in Fig. 3 (see Methods).

As shown in Fig. 3a, when pumping at 530 nm, Au nanoparticles supported on p-GaN (black squares) exhibit shorter $\tau_{e-\text{ph}}$ at all values of U_{abs} with a much smaller slope than those supported on Al_2O_3 (blue circles) or SiO_2 (blue triangles). Extrapolating each curve to zero U_{abs} yields a similar value of $\tau_{e-\text{ph}}$ for all samples of around 0.9 ps, which is consistent with previous observations from similarly sized Au nanoparticles^{14–18}. The nearly identical slope of $\tau_{e-\text{ph}}$ on both insulating supports, despite an ~30-fold lower thermal conductivity of SiO_2 relative to Al_2O_3 , confirms that the unique dynamics observed on p-GaN do not originate solely from differences associated with the thermal conductivity of the substrates. The much lower value of $\tau_{e-\text{ph}}$ observed from Au nanoparticles supported on p-GaN at all values of U_{abs} is indicative of a lower T_e in Au/p-GaN compared with Au/ Al_2O_3 or Au/ SiO_2 . We therefore attribute the markedly different relaxation dynamics observed on Au/p-GaN to the ultrafast hot-hole injection process, which does not occur on the two insulating supports.

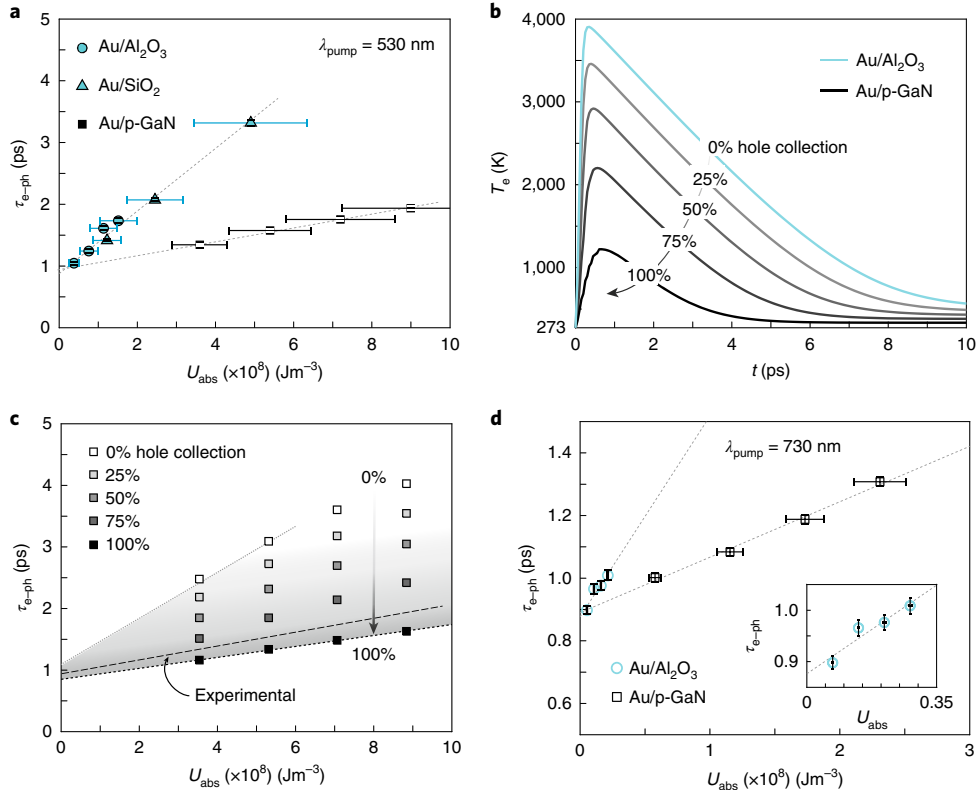


Fig. 3 | Influence of ultrafast hot-hole collection on the dynamics of hot electrons in Au nanoparticles. **a**, Experimentally derived values of electron-phonon coupling times ($\tau_{e\text{-ph}}$) as a function of absorbed energy density U_{abs} (J m^{-3}) for Au/p-GaN (black squares), Au/Al₂O₃ (blue circles) and Au/SiO₂ (blue triangles); the dashed lines serve as guides to the eye. Error bars represent the standard deviation of the mean particle volume. The slope of $\tau_{e\text{-ph}}$ for Au/p-GaN is $1.09 \times 10^{-9} \text{ ps m}^3 \text{ J}^{-1}$, and for Au/Al₂O₃ is $6.42 \times 10^{-9} \text{ ps m}^3 \text{ J}^{-1}$. **b**, Ab initio calculation showing the temporal evolution of the electronic temperature (T_e) after laser excitation at 530 nm ($U_{\text{abs}} = 5.3 \times 10^8 \text{ J m}^{-3}$) in Au/Al₂O₃ (blue curve) and Au/p-GaN (grey curves). For Au/p-GaN, the influence of removing hot holes 1 eV below the Au Fermi level is shown (light-grey curve: 25% → black curve: 100% hot-hole collection). **c**, Ab initio calculation of $\tau_{e\text{-ph}}$ as a function of absorbed energy density (U_{abs}) to show the influence of removing hot holes 1 eV below the Au Fermi level in Au/p-GaN (white squares: 0% → black squares: 100% hot-hole collection). The shaded region denotes the upper and lower bounds of computed $\tau_{e\text{-ph}}$ values. The slope of the experimental data points from panel **a** is also plotted (dashed black line) to aid comparison between theory and experiment. **d**, Experimentally derived values of $\tau_{e\text{-ph}}$ as a function of U_{abs} for Au/p-GaN (open black squares) and Au/Al₂O₃ (open blue circles) at a pump wavelength of 730 nm; the dashed lines serve as guides to the eye. Error bars represent the standard deviation of the mean. Inset: an enlarged view of the Au/Al₂O₃ data points. The slope of $\tau_{e\text{-ph}}$ for Au/p-GaN is $1.77 \times 10^{-9} \text{ ps m}^3 \text{ J}^{-1}$, while the slope of Au/Al₂O₃ remains unchanged.

Ab initio electronic structure calculations^{21,27–29} were then performed to further examine the influence of hot-hole injection on the thermalization dynamics of hot electrons in the Au nanoparticles (see Methods). As shown in Fig. 3b, removing hot holes from below the Au Fermi level on an ultrafast timescale indeed limits the peak electronic temperature attained in Au/p-GaN (grey-to-black curves) relative to Au/Al₂O₃ (blue curve), and further modifies the subsequent relaxation dynamics of hot electrons in the Au nanoparticles. The reduced T_e in Au/p-GaN is consistent with the observed difference in $\tau_{e\text{-ph}}$ between these two heterostructures (Fig. 3a). Theoretical estimation of $\tau_{e\text{-ph}}$ as a function of hot-hole collection at different absorbed energy densities (U_{abs}) further supports the interpretation of the experimentally observed trend: increased hot-hole collection reduces T_e of the electron gas, and therefore shortens $\tau_{e\text{-ph}}$ in the Au nanoparticles (Fig. 3c). The excellent quantitative agreement between the experimentally observed values of $\tau_{e\text{-ph}}$ (Fig. 3a) and that predicted from ab initio theory (Fig. 3c) confirms that our first-principles calculations accurately capture the relaxation dynamics of hot carriers without any adjustable parameters.

We can use the close correlation between experiment and theory to estimate the fraction of hot holes that are collected by p-GaN upon photo-excitation of the Au nanoparticles (see Methods).

To account for the markedly reduced value of $\tau_{e\text{-ph}}$ observed on Au/p-GaN would require that the majority ($\sim 88 \pm 8\%$) of hot holes reaching the Au/p-GaN interface with energies in excess of the Schottky barrier are injected into the p-GaN valence band (Fig. 3c, dashed black line). Such a high injection efficiency for hot holes substantially exceeds previously reported values for hot electrons^{19,20,22,23} and is consistent with theoretical predictions of the hot-hole energy distribution created upon interband excitation^{27,28}. Despite the large estimated injection efficiency, we note that the net change in the conduction electron density (ΔN_e) in the Au nanoparticles due to hot-hole injection is only $\sim 1\%$ because the number of photo-excited carriers is still a small fraction of the overall electron density (N_e) in the metal (Supplementary Fig. 4).

Influence of pump wavelength on hot electrons

Optical excitation of the Au nanoparticles at 530 nm ($h\nu = 2.34 \text{ eV}$) preferentially produces hot holes in the d bands of the metal³³, but a distribution of hot holes spanning the sp band is also present^{27,28}. To explore the contribution from injected sp -band holes to the change in thermalization dynamics observed on Au/p-GaN, additional experiments were performed at a pump wavelength of 730 nm ($h\nu = 1.70 \text{ eV}$). Note that this pump wavelength produces

hot holes with sufficient energy to surmount the Schottky barrier at the Au/p-GaN interface ($\Phi_b = 1.1$ eV), but they must arise from the *sp* bands of the metal; the *d* bands are inaccessible. As shown in Fig. 3d, pump-probe experiments performed at $\lambda_{\text{pump}} = 730$ nm also show differences in the slope of $\tau_{e-\text{ph}}$ between Au/p-GaN (black open squares) and Au/Al₂O₃ (blue open circles). Notably, however, relative to the Au/Al₂O₃ sample ($m = 6.42 \times 10^{-9} \text{ ps m}^3 \text{ J}^{-1}$), the relaxation dynamics of hot electrons on Au/p-GaN were not as noticeably altered when pumped at 730 nm ($m = 1.77 \times 10^{-9} \text{ ps m}^3 \text{ J}^{-1}$, Fig. 3d) as compared to 530 nm ($m = 1.09 \times 10^{-9} \text{ ps m}^3 \text{ J}^{-1}$, Fig. 3a). These results suggest that hot-hole injection from the Au *d* bands exerts a greater influence over the dynamics of hot electrons than that originating from the *sp* band. Indeed, photo-excitation above the interband threshold of Au is known to deposit most of the photon energy in hot holes that are more than 2 eV below the Fermi level²⁹. Removing these hot holes on ultrafast timescales via injection into p-GaN is anticipated to eliminate a substantial fraction of the absorbed energy from the electron gas.

To explain the experimental observations requires an understanding of the complex interplay between the wavelength-dependent energetics of hot holes, their associated velocities and their injection probability over the Schottky barrier. Figure 4a,b shows first-principles predictions of the energy (Fig. 4a) and velocity (Fig. 4b) distributions of hot carriers generated by pump energies above (2.34 eV, solid curves) and below (1.70 eV, dashed curves) the interband threshold of Au (~1.8 eV). As shown in Fig. 4a, the distributions exhibit nearly uniform probability, extending from the Au Fermi level up to the photon energy of both electrons and holes for indirect transitions (dashed curve). In contrast, a much narrower distribution of high-energy holes peaked around the *d* bands accompanied by low-energy electrons centred just above the Au Fermi level is created via direct transitions (solid curve). Figure 4b shows that the *d*-band holes possess lower relative velocities than the more mobile *sp*-band holes produced via indirect transitions (holes shown with negative velocity only as a visual aid to separate them from the electrons). Despite the bimodal velocity distributions between *sp*-band and *d*-band holes (Fig. 4b), we emphasize that a sizeable fraction of hot holes retains a sufficiently high velocity to enable transport to the Au/p-GaN interface upon photo-excitation at 530 nm ($h\nu = 2.34$ eV). Combining the hot-carrier energy distributions with their associated velocities allows for computing the flux of hot holes impinging upon the Au/p-GaN interface normalized by U_{abs} (Fig. 4c, dashed black curve). Interestingly, the lower carrier velocity of *d*-band holes compared to *sp*-band holes results in a relatively constant flux of hot holes across the visible regime.

Obtaining the subset of hot holes that are successfully transferred to p-GaN from those that merely reach the interface requires knowledge of the wavelength-dependent injection efficiency for hot holes across the Au/p-GaN interface. To this end, we fabricated Au/p-GaN hot-hole photodiodes (see Methods and Supplementary Figs. 5a–c) and evaluated the internal quantum efficiency (IQE) of hot-hole injection (Supplementary Fig. 5d). Combining ab initio calculations with the experimentally measured IQE allows determination of the hot-hole injection efficiency (Supplementary Fig. 5e). Finally, we computed the flux of hot holes that reached the Au/p-GaN interface and were successfully injected into the p-GaN valence band (Fig. 4c, solid black curve). The obtained plot of the injected hot-hole flux reveals the combined influence of both carrier energy and velocity on the hole-injection probability at the Au/p-GaN interface. Although a similar flux of high mobility *sp*-band holes and less mobile *d*-band holes impinges upon the interface (Fig. 4c, dashed black curve), the lower energies of *sp*-band holes relative to their *d*-band counterparts limit their injection probability across the Schottky barrier (Fig. 4c, solid black curve). Overall, these theoretical predictions qualitatively capture the observed experimental trends: ultrafast hot-hole injection from the *sp* band of the

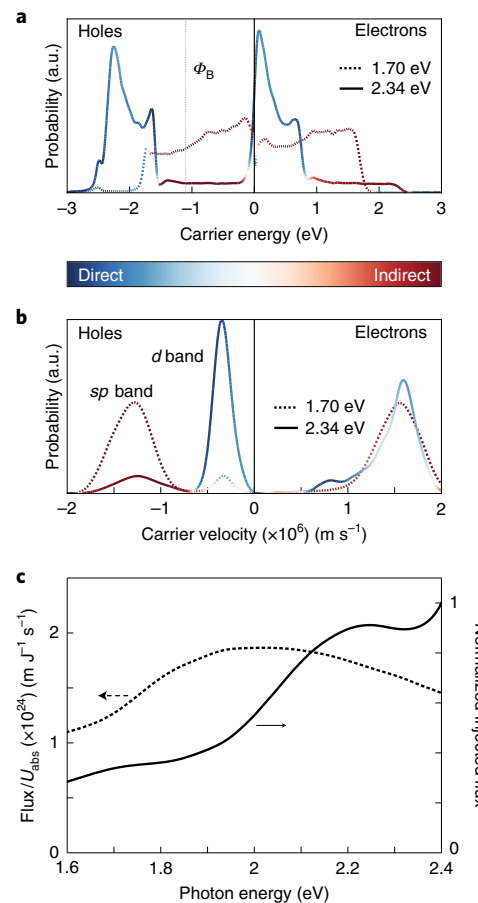


Fig. 4 | Influence of incident pump wavelength on hot-hole injection at the Au/p-GaN interface. **a**, Ab initio calculation of the energy distributions of hot electrons (positive energies) and hot holes (negative energies) produced on the Au nanoparticles at a pump wavelength of 530 nm ($h\nu = 2.34$ eV, solid lines) and 730 nm ($h\nu = 1.70$ eV, dashed lines). The vertical dashed line denotes the Schottky barrier ($\Phi_b = 1.1$ eV) at the Au/p-GaN interface. The colour scale indicates the relative contribution from direct (blue) and indirect (red) electronic transitions and applies to panels **a** and **b**. **b**, Ab initio calculation of the velocity distributions of hot electrons and hot holes produced on the Au nanoparticles at a pump wavelength of 530 nm (solid lines) and 730 nm (dashed lines). Negative velocities of hot holes used only as a visual aid to distinguish them from the hot electrons. **c**, Ab initio calculation of the total flux of hot holes impinging upon the Au/p-GaN interface as a function of incident photon energy normalized by the absorbed energy density, U_{abs} (dashed black curve, left ordinate axis). The solid black curve (right ordinate axis) represents the relative number of hot holes that reach the interface and are successfully injected into the p-GaN valence band. a.u., arbitrary units.

metal is capable of modifying the thermalization dynamics of hot electrons, but to a lesser extent than from the *d* bands, because the Schottky barrier limits their injection probability upon reaching the Au/p-GaN interface.

Summary and outlook

Figure 5a shows the calculated peak electronic temperature ($T_{e,\text{peak}}$) established after photon absorption plotted as a function of hot-hole collection from the Au nanoparticles for various absorbed energy densities (U_{abs}). These curves indicate that $T_{e,\text{peak}}$ is increasingly limited with increasing hot-hole collection efficiency at the Au/p-GaN interface (Fig. 5a). A summary of how hot-hole injection influences

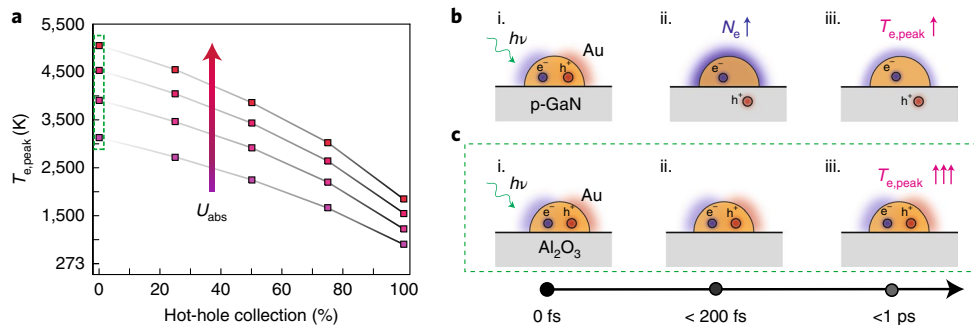


Fig. 5 | Comparison of ultrafast hot-carrier dynamics in Au nanoparticles supported on p-GaN and Al₂O₃ substrates. **a**, Ab initio calculation of the peak electronic temperature (T_e) established in Au/p-GaN (red squares) for various absorbed energy densities (U_{abs}) plotted as a function of the total percentage of hot holes more than 1 eV below the Au Fermi level that are collected from the Au nanoparticles by the p-GaN support. **b,c**, Schematic representation of hot-electron dynamics occurring on the Au nanoparticles with (**b**) and without (**c**) hot-hole collection by the underlying substrate. Optical excitation creates hot electrons (blue, e^-) and hot holes (red, h^+) on the metal (**b(i),c(i)**). Ultrafast ($t < 200$ fs) hot-hole injection in Au/p-GaN heterostructures increases the electron density (N_e) of the Au nanoparticles on timescales commensurate with electron-electron scattering (**b(ii)**), while hot carrier separation is forbidden on an insulating substrate like Al₂O₃ (**c(ii)**). As a result, a lower electronic temperature (T_e) of the electron gas is observed on Au/p-GaN heterostructures (**b(iii)**) relative to that of Au/Al₂O₃ heterostructures (**c(iii)**). The horizontal black arrow indicates the approximate timescales (t) for these processes to occur on the Au nanoparticle.

the thermalization dynamics of hot electrons occurring on Au/p-GaN heterostructures relative to Au/Al₂O₃ is depicted schematically in Fig. 5b,c. A hot-carrier population consisting of hot electrons (e^- , blue circles) and hot holes (h^+ , red circles) is initially produced on the Au surface via photon absorption at time (t) zero (Fig. 5b(i),c(i)). On p-GaN supports, the majority of hot holes generated in the Au nanoparticles with energies in excess of the Schottky barrier are injected into the p-GaN valence band in less than 200 fs (Fig. 5b(ii)). This increased electron density (N_e) on the Au nanoparticles raises the electronic heat capacity (C_e) of the electron gas in the Au/p-GaN heterostructures (Fig. 5b(ii)) relative to Au/Al₂O₃ (Fig. 5c(ii)), in which charge separation is prohibited. The electronic temperature (T_e) of each system is subsequently increased via electron–electron scattering, but the elevated C_e of the Au/p-GaN system results in a lower T_e (Fig. 5b(iii)) relative to that observed on Au/Al₂O₃ (Fig. 5c(iii)).

In summary, we have observed ultrafast ($t < 200$ fs) hot-hole injection from Au nanoparticles to the valence band of p-GaN, placing hot-hole transfer on similar timescales as hot-electron transfer^{22,23}. Excellent quantitative agreement between experiment and ab initio theory suggests that nearly 90% of hot holes possessing enough energy to surmount the Schottky barrier ($\Phi_B = 1.1$ eV) at the Au/p-GaN interface are collected by the p-GaN support. Together with the relatively long lifetime of the charge-separated state ($t \approx ns$), these observations suggest that hot-hole-based optoelectronics could offer comparable, if not improved, device performance relative to that obtained with hot-electron-based systems. Particularly for photodetectors that operate via hot-hole collection, the apparent high efficiency of hot-hole injection from the metal nanoantenna is anticipated to provide better responsivity at shorter wavelengths relative to devices that operate via hot-electron collection. We also demonstrate that selectively extracting hot holes from below the Au Fermi level on timescales commensurate with electron–electron scattering considerably alters the relaxation dynamics of hot electrons. Overall, these observations suggest the potential for manipulating the electronic temperature of hot carriers on metal nanostructures by collecting hot holes from the metal on ultrafast timescales. Such a strategy may enable shaping the energy distributions of hot electrons in metal nanostructures by tailoring the occupation of states above the metal Fermi level to control the selectivity of photochemical reactions.

Online content

Any methods, additional references, Nature Research reporting summaries, source data, extended data, supplementary information, acknowledgements, peer review information; details of author contributions and competing interests; and statements of data and code availability are available at <https://doi.org/10.1038/s41563-020-0737-1>.

Received: 6 December 2018; Accepted: 16 June 2020;

Published online: 27 July 2020

References

- Clavero, C. Plasmon-induced hot-electron generation at nanoparticle/metal-oxide interfaces for photovoltaic and photocatalytic devices. *Nat. Photon.* **8**, 95–103 (2014).
- Brongersma, M. L., Halas, N. J. & Nordlander, P. Plasmon-induced hot carrier science and technology. *Nat. Nanotechnol.* **10**, 25–34 (2015).
- Christopher, P. & Moskovits, M. Hot charge carrier transmission from plasmonic nanostructures. *Annu. Rev. Phys. Chem.* **68**, 379–398 (2017).
- Aslam, U., Rao, V. G., Chavez, S. & Linic, S. Catalytic conversion of solar to chemical energy on plasmonic metal nanostructures. *Nat. Catal.* **1**, 656–665 (2018).
- Linic, S., Christopher, P. & Ingram, D. B. Plasmonic-metal nanostructures for efficient conversion of solar to chemical energy. *Nat. Mater.* **10**, 911–921 (2011).
- Knight, M. W., Sobhani, H., Nordlander, P. & Halas, N. J. Photodetection with active optical antennas. *Science* **332**, 702–704 (2011).
- Zheng, B. Y. et al. Distinguishing between plasmon-induced and photoexcited carriers in a device geometry. *Nat. Commun.* **6**, 7797 (2015).
- Li, W. et al. Circularly polarized light detection with hot electrons in chiral plasmonic metamaterials. *Nat. Commun.* **6**, 8379 (2015).
- Tagliabue, G. et al. Quantifying the role of surface plasmon excitation and hot carrier transport in plasmonic devices. *Nat. Commun.* **9**, 3394 (2018).
- Mubeen, S. et al. An autonomous photosynthetic device in which all charge carriers derive from surface plasmons. *Nat. Nanotechnol.* **8**, 247–251 (2013).
- Mubeen, S., Lee, J., Liu, D., Stucky, G. D. & Moskovits, M. Panchromatic photoproduction of H₂ with surface plasmons. *Nano Lett.* **15**, 2132–2136 (2015).
- Zhou, L. et al. Quantifying hot carrier and thermal contributions in plasmonic photocatalysis. *Science* **362**, 69–72 (2018).
- Christopher, P., Xin, H. & Linic, S. Visible-light-enhanced catalytic oxidation reactions on plasmonic silver nanostructures. *Nat. Chem.* **3**, 467–472 (2011).
- Link, S. & El-Sayed, M. A. Optical properties and ultrafast dynamics of metallic nanoparticles. *Annu. Rev. Phys. Chem.* **54**, 331–366 (2003).
- Hartland, G. V. Optical studies of dynamics in noble metal nanostructures. *Chem. Rev.* **111**, 3858–3887 (2011).

16. Hodak, J. H., Martini, I. & Hartland, G. V. Spectroscopy and dynamics of nanometer-sized noble metal nanoparticles. *J. Phys. Chem. B* **102**, 6958–6967 (1998).
17. Hodak, J. H., Henglein, A. & Hartland, G. V. Electron-phonon coupling dynamics in very small (between 2 and 8 nm diameter) Au nanoparticles. *J. Chem. Phys.* **112**, 5942–5947 (2000).
18. Link, S. & El-Sayed, M. A. Spectral properties and relaxation dynamics of surface plasmon electronic oscillations in gold and silver nanodots and nanorods. *J. Phys. Chem. B* **103**, 8410–8426 (1999).
19. Wu, K., Rodriguez-Cordoba, W. E., Yang, Y. & Lian, T. Plasmon-induced hot electron transfer from the Au tip to CdS rod in CdS-Au nanoheterostructures. *Nano Lett.* **13**, 5255–5263 (2013).
20. Wu, K., Chen, J., McBride, J. R. & Lian, T. Efficient hot-electron transfer by a plasmon-induced interfacial charge-transfer transition. *Science* **349**, 632–635 (2015).
21. Brown, A. M. et al. Experimental and ab initio ultrafast carrier dynamics in plasmonic nanoparticles. *Phys. Rev. Lett.* **118**, 087401 (2017).
22. Furube, A., Du, L., Hara, K., Katoh, R. & Tachiya, M. Ultrafast plasmon-induced electron transfer from gold nanodots into TiO₂ nanoparticles. *J. Am. Chem. Soc.* **129**, 14852–14853 (2007).
23. Ratchford, D. C., Dunkerlberger, A. D., Vurgaftman, I., Owrutsky, J. C. & Pehrsson, P. E. Quantification of efficient plasmonic hot-electron injection in gold nanoparticle-TiO₂ films. *Nano Lett.* **17**, 6047–6055 (2017).
24. Harutyunyan, H. et al. Anomalous ultrafast dynamics of hot plasmonic electrons in nanostructures with hot spots. *Nat. Nanotechnol.* **10**, 770–774 (2015).
25. Tan, S. et al. Plasmonic coupling at a metal/semiconductor interface. *Nat. Photon.* **11**, 806–812 (2018).
26. Bauer, M., Marienfeld, A. & Aeschlimann, M. Hot electron lifetimes in metals probed by time-resolved two-photon photoemission. *Prog. Surf. Sci.* **90**, 319–376 (2015).
27. Brown, A. M., Sundaraman, R., Narang, P., Goddard, W. A. III & Atwater, H. A. Nonradiative plasmon decay and hot carrier dynamics: effects of phonons, surfaces, and geometry. *ACS Nano* **10**, 957–966 (2016).
28. Sundaraman, R., Narang, P., Jermyn, A. S., Goddard, W. A. III & Atwater, H. A. Theoretical predictions for hot-carrier generation from surface plasmon decay. *Nat. Commun.* **5**, 5788 (2014).
29. Brown, A. M., Sundaraman, R., Narang, P., Goddard, W. A. III & Atwater, H. A. Ab initio phonon coupling and optical response of hot electrons in plasmonic metals. *Phys. Rev. B* **94**, 075120 (2016).
30. DuChene, J. S., Tagliabue, G., Welch, A. J., Cheng, W.-H. & Atwater, H. A. Hot hole collection and photoelectrochemical CO₂ reduction with plasmonic Au/p-GaN photocathodes. *Nano Lett.* **18**, 2545–1550 (2018).
31. Matsui, T. et al. Highly stable plasmon induced hot hole transfer into silicon via a SrTiO₃ passivation interface. *Adv. Funct. Mater.* **28**, 1705829 (2018).
32. Lian, Z. et al. Near infrared light induced plasmonic hot hole transfer at a nano-heterointerface. *Nat. Commun.* **9**, 2314 (2018).
33. Sá, J. et al. Direct observation of charge separation on Au localized surface plasmons. *Energy Environ. Sci.* **6**, 3584–3588 (2013).
34. Ye, H., Wicks, G. W. & Fauchet, P. M. Hot hole relaxation dynamics in p-GaN. *Appl. Phys. Lett.* **77**, 1185 (2000).

Publisher's note Springer Nature remains neutral with regard to jurisdictional claims in published maps and institutional affiliations.

© The Author(s), under exclusive licence to Springer Nature Limited 2020

Methods

Fabrication of Au/p-GaN, Au/Al₂O₃ and Au/SiO₂ heterostructures. The Au/p-GaN heterostructures were constructed via evaporation of Au thin films onto commercial p-type GaN on sapphire substrates (Pam-Xiamen). Immediately before Au evaporation, the p-GaN substrates were pretreated with dilute NH₄OH solution (0.02% v/v%) for 30 s to remove any native oxide, followed by 30 s of copious washing in Nanopure water. The p-GaN/sapphire substrate was then blown dry with N₂ gas and loaded into the vacuum chamber. A 1.5-nm-thick film of Au was deposited onto the p-GaN surface using electron-beam physical vapour deposition at a base pressure of $\sim 1 \times 10^{-7}$ torr and a deposition rate of 1.0 Å s⁻¹. The Au/p-GaN films were then annealed in ambient air at 300 °C for 1 h to ensure coalescence of the discontinuous Au thin film into Au nanoparticles and to achieve good adhesion with the underlying p-GaN surface. Note that no interfacial adhesion layer was used to construct the Au/p-GaN heterojunction. The control samples (Au/Al₂O₃, Au/SiO₂ and Au/ZrO₂) were prepared the same way as the Au/p-GaN heterostructures described above, except that sapphire (Al₂O₃), glass (SiO₂) or zirconia (ZrO₂) were used as the substrate. The Al₂O₃ (MTI, sapphire wafer, c-plane, 2sp), SiO₂ substrates (VWR soda-lime glass) or ZrO₂ substrates were sequentially cleaned with acetone, isopropanol and then water for 5 min each, while sonicating in a water bath. The substrates were then copiously rinsed with water and blown dry with N₂ gas before loading into the vacuum chamber for Au deposition. No interfacial adhesion layer was used for the Au/Al₂O₃, Au/SiO₂ or Au/ZrO₂ heterostructures.

Ultrafast transient absorption spectroscopy experiments. The detection of ultrafast hot-hole injection to the p-GaN valence band was monitored via transient infrared absorption spectroscopy (TIRAS). TIRAS experiments were carried out in a femtosecond transient absorption spectrometer (Helios IR, Ultrafast Systems LLC) at room temperature. Briefly, the output of a Ti:sapphire amplifier with integrated oscillator and pump lasers (800 nm, 40 fs, 3 kHz, Libra LHE, Coherent) was split into two beams, which were used to pump two TOPAS Prime optical parametric amplifiers coupled with frequency mixers (Light Conversion). This setup produced a depolarized visible pump pulse ($\lambda_{\text{pump}} = 530$ nm) and a broad mid-infrared probe spectrum ($\lambda_{\text{probe}} = 1,850\text{--}2,200\text{ cm}^{-1}$). Pump pulse energies were adjusted using a neutral density filter placed before the sample. The laser spot size for the 530-nm pump was $\sim 120 \times 160\text{ }\mu\text{m}^2$. Before reaching the sample, the probe beam was split into equal-intensity probe and reference beams. The detection of probe and reference beams was done using a femtosecond transient absorption spectrometer (Helios IR, Ultrafast Systems LLC). The instrument response function for the experiments was approximately 200 fs. All the films were measured in a Specac cell. The samples were moved manually during the measurements to minimize possible laser-induced sample damage.

The hot-electron dynamics on the Au nanoparticles were monitored with femtosecond transient absorption spectroscopy across the visible regime. Measurements were performed at the Center for Nanoscale Materials, Argonne National Laboratory using an amplified Ti:sapphire laser system (Spectra Physics, Spitfire Pro) and an automated data acquisition system (Ultrafast Systems, HELIOS). The output of the amplified laser (800 nm, 150 fs, 5 kHz) was split 90:10, with the majority used to pump an optical parametric amplifier (Light Conversion, TOPAS), which provided the pump beam ($\lambda_{\text{pump}} = 530$ nm). The remaining 10% was used to make the probe beam ($\lambda_{\text{probe}} = 450\text{--}750$ nm) after traversing an optical delay line by focusing into a 2-mm-thick sapphire window. The probe continuum was passed through a 785-nm short-pass filter (Semrock) to remove residual 800 nm and longer wavelengths of light. The pump and probe beams were focused ($\sim 180\text{ }\mu\text{m}$ diameter at full width half maximum (FWHM)) and overlapped on the sample. Pump energies ranged from 100 to 600 μW (0.16–0.96 mJ cm⁻²). Four scans covering 50 ps were collected and averaged, with no sample degradation detected.

Ab initio theoretical calculations. We predicted the evolution of electron temperature T_e using first-principles calculations of carrier excitation by the pump pulse, electron thermalization by electron–electron (e–e) scattering as well as relaxation by electron–phonon (e–ph) coupling. We performed density functional theory calculations of electron and phonon states, and their interaction matrix elements in the open-source JDFTx software³⁵. Using Fermi’s golden rule in an efficient Wannier representation^{27,28}, we then calculated the initial hot-carrier distributions as well as the collision integrals necessary for solving the Boltzmann transport equation for the evolution of the electron distribution²¹. Within this Wannier framework, we also calculated carrier velocities for each electronic state and histogram the Fermi golden rule calculations for carrier generation by velocities to compute the carrier velocity distributions excited by each photon energy. Similarly, we also weighted the energy distribution histograms by carrier velocities to calculate carrier flux resolved by carrier energies for each photon energy of excitation. Integrating over this energy-resolved flux for carrier energies above the Schottky barrier, or additionally weighted by experimentally estimated carrier injection probabilities $P_{\text{inj}}(\epsilon)$ (see below), we estimated the total carrier flux impinging upon the interface with energies above the Schottky barrier and the flux injected across the interface, respectively.

Briefly, for the transport simulations, the initial carrier distribution following excitation by the pump is

$$f(\epsilon, t=0) = f_0(\epsilon) + U_{\text{abs}} \frac{P(\epsilon, \hbar\omega, P_{\text{inj}})}{g(\epsilon)},$$

where f_0 is the Fermi distribution at equilibrium, U_{abs} is the pump energy absorbed density, $g(\epsilon)$ is the electronic density of states and $P(\epsilon, \hbar\omega, P_{\text{inj}})$ is the energy distribution of carriers excited by a photon energy of $\hbar\omega$. Here, P_{inj} is the percentage of holes greater than 1 eV below the Fermi level that are injected into the substrate (only for the p-GaN case). The absorbed pump energy density U_{abs} is determined by the nanoparticle size, beam diameter, pump pulse energy and the steady-state absorption coefficient of the sample (see below).

Evolution of the carrier distribution with time t is then captured by the nonlinear Boltzmann equation:

$$\frac{d}{dt}f(\epsilon, t) = \Gamma_{e-e}[f](\epsilon) + \Gamma_{e-ph}[f, T_l](\epsilon),$$

where Γ_{e-e} and Γ_{e-ph} are the collision integrals for e–e and e–ph scattering, determined fully from first principles exactly as detailed in ref.²¹, and T_l is the lattice temperature. From the predicted distribution function $f(\epsilon)$ at each time t , we estimate the electron temperature T_e from the derivative of $f(\epsilon)$ at the Fermi energy, because this correlates well with the dominant change in the optical response due to a large number of lower energy carriers near the Fermi level³⁹. Finally, we predict the electron–phonon relaxation time, τ_{e-ph} , from the fall time of the calculated electron temperature, which is in excellent agreement with fall times extracted from ultrafast transient absorption experiments. To estimate the injection efficiency η , we use the calculated values of τ_{e-ph} as a function of U_{abs} and η . Specifically, we sample 1,000 τ_{e-ph} and U_{abs} from normal distributions of each experimental data point using the error estimates as standard deviations, compute η for each sample by interpolation on the computational results and report the mean and standard deviation of the η samples as the experimental efficiency estimate with error bars.

The Au/p-GaN, Au/Al₂O₃ and Au/SiO₂ heterostructures exhibit different particle diameter, area coverage and optical absorption. Although the electron–phonon coupling constant is known to be independent of size for metal nanoparticles in the size regime studied here ($d=7\text{--}15\text{ nm}$)^{14–18}, the observed thermalization dynamics at a given pump power are proportional to the electronic temperature of the photo-excited electron gas of the metal nanoparticles. A fair comparison between the different heterostructures can thus be obtained only on the basis of the energy absorbed per unit volume of gold, U_{abs} (J m⁻³). We determine U_{abs} according to the following expression:

$$U_{\text{abs}} (\text{J m}^{-3}) = \frac{\text{energy absorbed per nanoparticle}}{\text{nanoparticle volume}} = \frac{\left(\frac{\text{Abs}_{530} E_{\text{pulse}}}{\pi r_{\text{beam}}^2} \times \frac{\pi r_{\text{NP}}^2}{C} \right)}{\frac{4}{3} \pi r_{\text{NP}}^3}$$

where Abs_{530} is the steady-state absorption at 530 nm (11.7% for Au/p-GaN, 8.7% for Au/Al₂O₃ and 13.1% for Au/SiO₂), E_{pulse} is the pump pulse energy (0.4–2.0 × 10⁻⁷ J per pulse for 100–500 μW), $2r_{\text{NP}}$ is the nanoparticle diameter (7.3 nm for Au/p-GaN, 12.2 nm for Au/Al₂O₃ and 14.7 nm for Au/SiO₂), C is the nanoparticle area coverage (18.7% for Au/p-GaN, 38.8% for Au/Al₂O₃ and 13.7% for Au/SiO₂) and $2r_{\text{beam}}$ is the pump beam diameter ($\sim 180\text{ }\mu\text{m}$ FWHM). The average size of the Au nanoparticles, and hence the experimental U_{abs} for each sample, was obtained by analysis of scanning electron microscopy (SEM) images of Au/p-GaN using ImageJ software and atomic force microscopy scans for Au/Al₂O₃ and Au/SiO₂ using the Gwyddion software package. In each case, there is an uncertainty associated with the initial choice of the threshold value for identifying particles using the ‘Particle Analysis’ function or the ‘Grain Size Distribution’ function in the software packages. Therefore, on several images of each sample, we repeatedly determined the mean diameter using a slightly different threshold for which visual inspection of the identified nanoparticle region gave an acceptable result. The mean diameter used to calculate U_{abs} for each sample was then the average of the repeated analysis above, and the uncertainty in U_{abs} was determined from the standard deviation of the mean nanoparticle diameter.

Fabrication and characterization of solid-state Au/p-GaN photodiodes. Devices were fabricated and characterized according to the protocols outlined in ref.⁹. We emphasize that exactly the same surface treatment steps that were used for the Au/p-GaN heterostructures (described above) were applied to the solid-state Au/p-GaN photodiodes. Moreover, no interfacial adhesion layer was used between the Au nanoantennas and the p-GaN support, to ensure that the interface is identical between the two Au/p-GaN heterostructures. From measured internal quantum efficiency IQE(ω) as a function of photon energy, we estimate the carrier-energy-resolved carrier injection probability $P_{\text{inj}}(\epsilon)$ by inverting the relation,

$$\text{IQE}(\omega) = \int_{\Phi_B}^{\hbar\omega} P_{\text{inj}}(\epsilon) P_{\text{gen}}(\epsilon, \omega) d\epsilon$$

where $P(\omega, \epsilon)$ is the probability density that a photon of energy $\hbar\omega$ generates a carrier of energy ϵ , calculated from first principles using the Wannier framework

described above (accounting for direct and phonon-assisted excitations). To carry out this inversion in a numerically stable way, we assume that the IQE contributions in the p-GaN device only arise from hole injection. We correspondingly assume $P_{\text{inj}}(\epsilon)$ to be non-zero only for hole energies above the Schottky barrier Φ_B (that is, $\epsilon < -\Phi_B$). We then assume the $P_{\text{inj}}(\epsilon)$ to be a smooth function of ϵ , represented as a cubic spline, and convert the above integrals to a system of linear equations of the spline control points. Finally, we solve those equations using a least-squares method to effectively fit $P_{\text{inj}}(\epsilon)$ to the experimentally measured IQE based on ab initio predictions of hot-carrier distributions.

Data availability

The datasets generated and analysed during the study are available from the corresponding authors upon request.

References

35. Sundaraman, R. et al. JDFTx: software for joint density-functional theory. *SoftwareX* **6**, 278–284 (2017).

Acknowledgements

This material is based upon work performed by the Joint Center for Artificial Photosynthesis, a DOE Energy Innovation Hub, supported through the Office of Science of the US Department of Energy under award no. DE-SC0004993. A portion of the ultrafast spectroscopy work was performed at the Center for Nanoscale Materials, a US Department of Energy Office of Science User Facility, and supported by the US Department of Energy, Office of Science, under contract no. DE-AC02-06CH11357. G.T.

acknowledges support from the Swiss National Science Foundation through the Early Postdoc.Mobility Fellowship, grant no. P2EZP2_159101 and the Advanced Mobility Fellowship, grant no. P300P2_171417. We also thank M. V. Pavliuk for assistance in conducting ultrafast transient absorption spectroscopy measurements from planar Au films on p-GaN substrates.

Author contributions

J.S.D., G.T. and H.A.A. conceived the idea, designed the experiments, analysed data and wrote the manuscript with contributions from all authors. M.A., Y.H. and J.S. performed infrared transient absorption spectroscopy experiments. M.A., K.Z., S.E.C. and D.J.G. performed visible transient absorption spectroscopy experiments. A.H. and R.S. performed ab initio theory calculations. J.S.D. and G.T. fabricated and characterized materials. W.-H.C. acquired absorption spectra of materials. H.A.A. supervised the project. All authors have given approval to the final version of the manuscript.

Competing interests

The authors declare no competing interests.

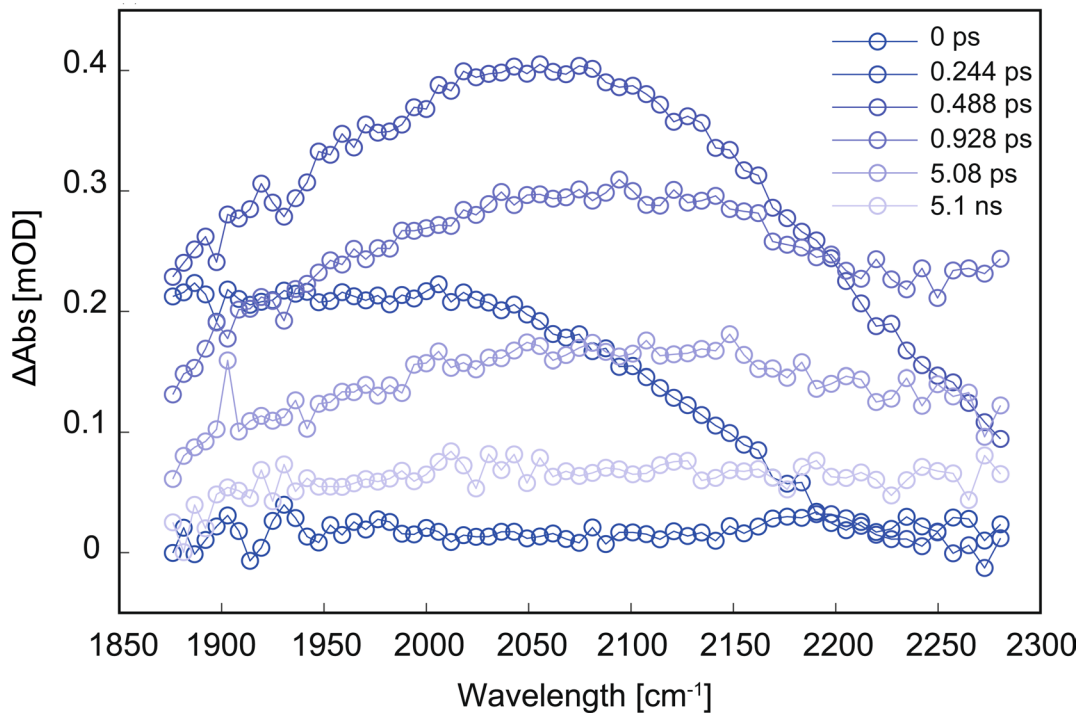
Additional information

Extended data is available for this paper at <https://doi.org/10.1038/s41563-020-0737-1>.

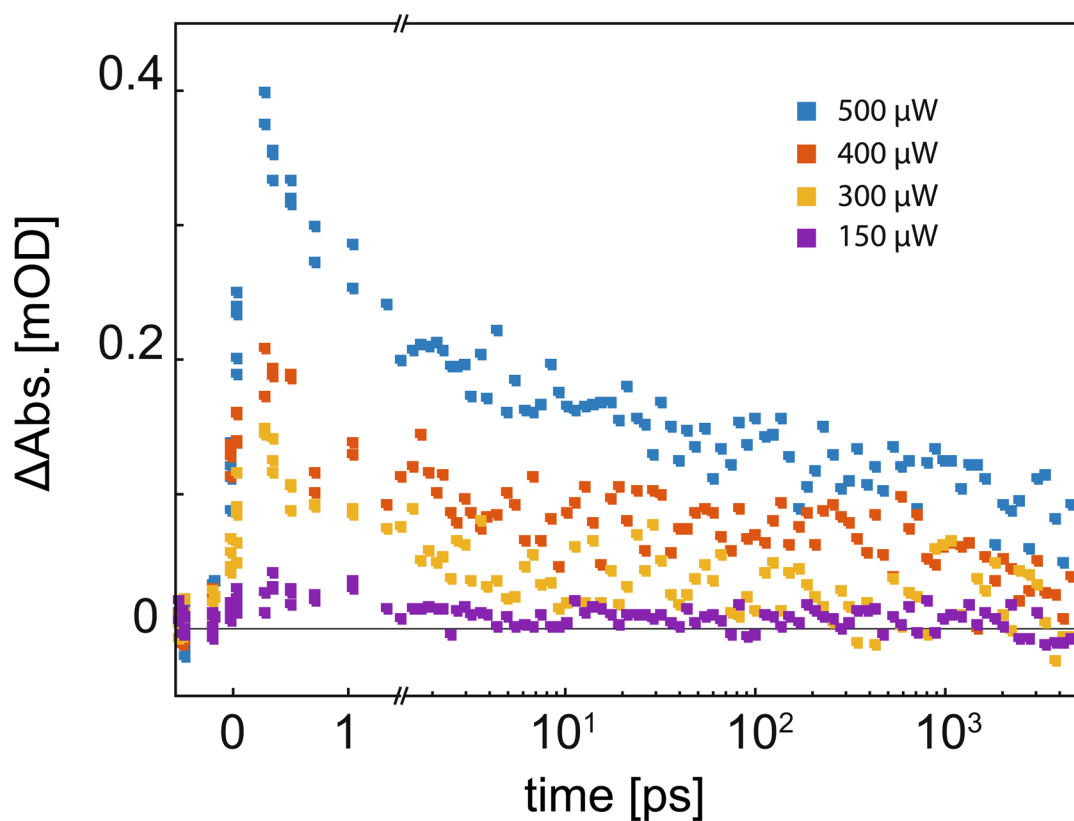
Supplementary information is available for this paper at <https://doi.org/10.1038/s41563-020-0737-1>.

Correspondence and requests for materials should be addressed to J.S. or H.A.A.

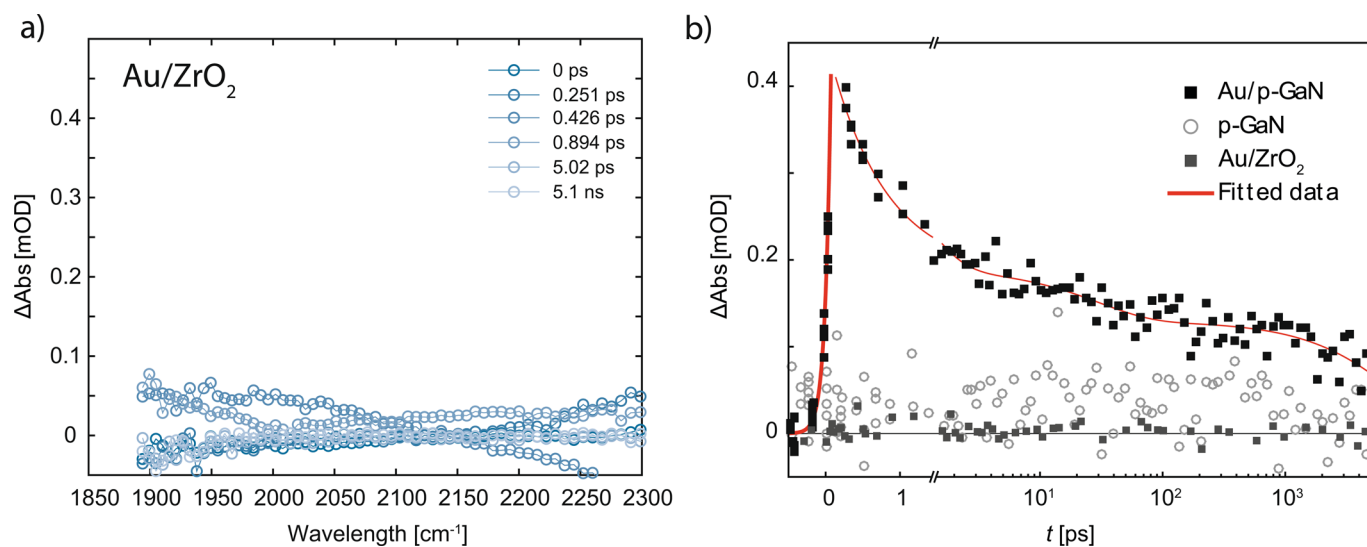
Reprints and permissions information is available at www.nature.com/reprints.



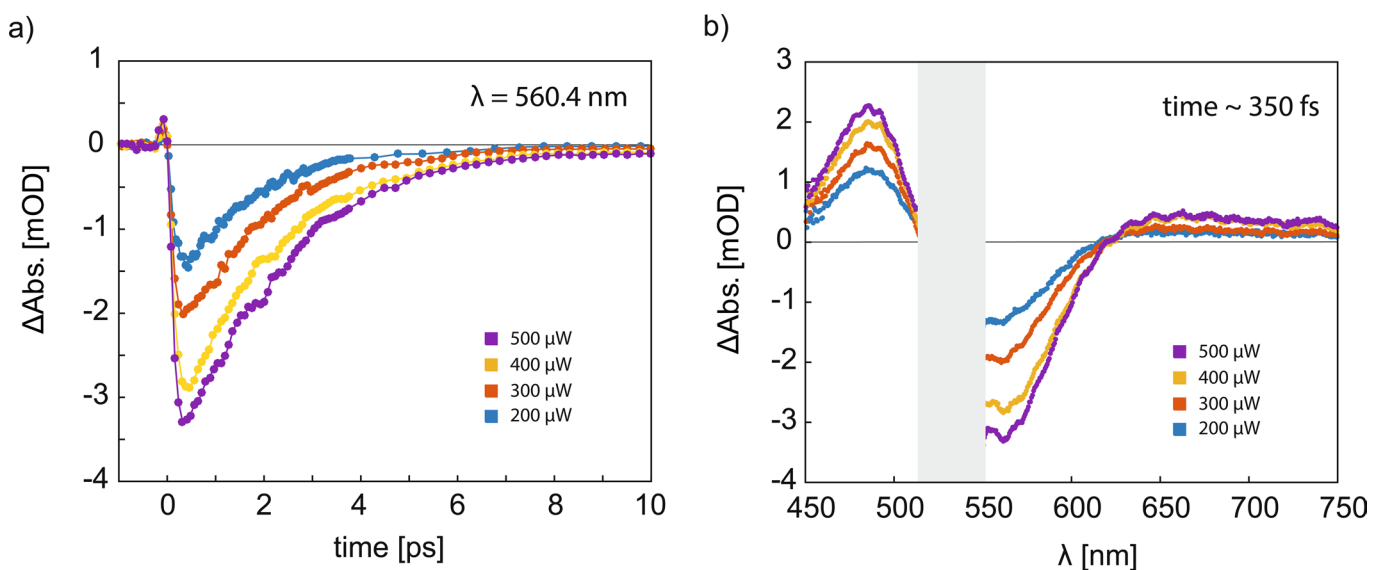
Extended Data Fig. 1 | Transient infrared absorption spectroscopy of Au/p-GaN heterostructures. Full infrared probe spectrum ($\lambda_{\text{probe}} = 1850\text{--}2250 \text{ cm}^{-1}$) obtained from Au/p-GaN upon 530 nm pump pulse at an incident power of 400 μW . The plot shown in Fig. 2b shows the temporal rise and decay taken at 2060 cm^{-1} ($\lambda_{\text{probe}} = 4.85 \mu\text{m}$).



Extended Data Fig. 2 | Power-dependent transient infrared absorption spectroscopy of Au/p-GaN heterostructures. Ultrafast transient rise and decay probed at 2060 cm^{-1} ($\lambda_{\text{probe}} = 4.85 \mu\text{m}$) obtained from Au/p-GaN upon 530 nm pump pulse at several different incident powers.

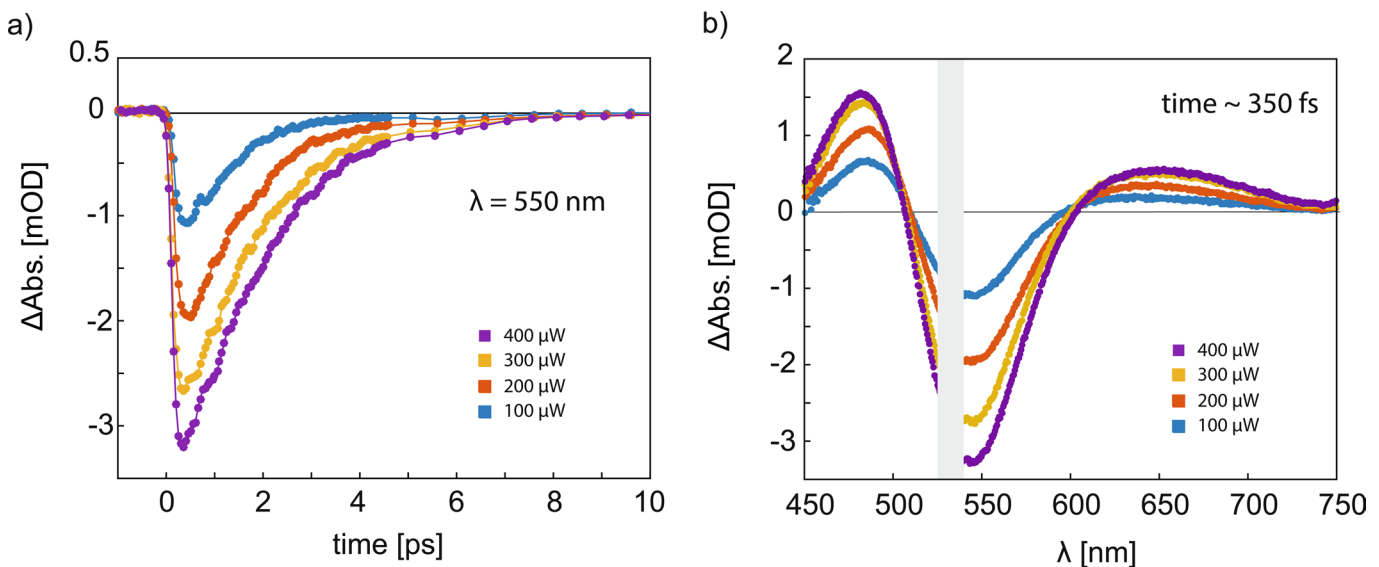


Extended Data Fig. 3 | Transient infrared absorption spectroscopy of Au/ZrO_2 heterostructures. **a**, Full infrared probe spectrum ($\lambda_{\text{probe}} = 1900\text{--}2300\text{ cm}^{-1}$) obtained from Au/ZrO_2 upon 530 nm pump pulse at an incident power of 500 μW . **b**, Ultrafast transient rise and decay probed at 2060 cm^{-1} ($\lambda_{\text{probe}} = 4.85\text{ }\mu\text{m}$) obtained from $\text{Au}/\text{p-GaN}$ (black points), bare p-GaN (open circles), and Au/ZrO_2 (grey points) upon 530 nm pump pulse at an incident power of 500 μW ($\text{Au}/\text{p-GaN}$ and Au/ZrO_2) and 750 μW (bare p-GaN). The red line shows a fit to the experimental $\text{Au}/\text{p-GaN}$ data, which exhibits an instrument-limited rise time of less than 200 fs. No signal was obtained from either bare p-GaN or Au/ZrO_2 heterostructures.



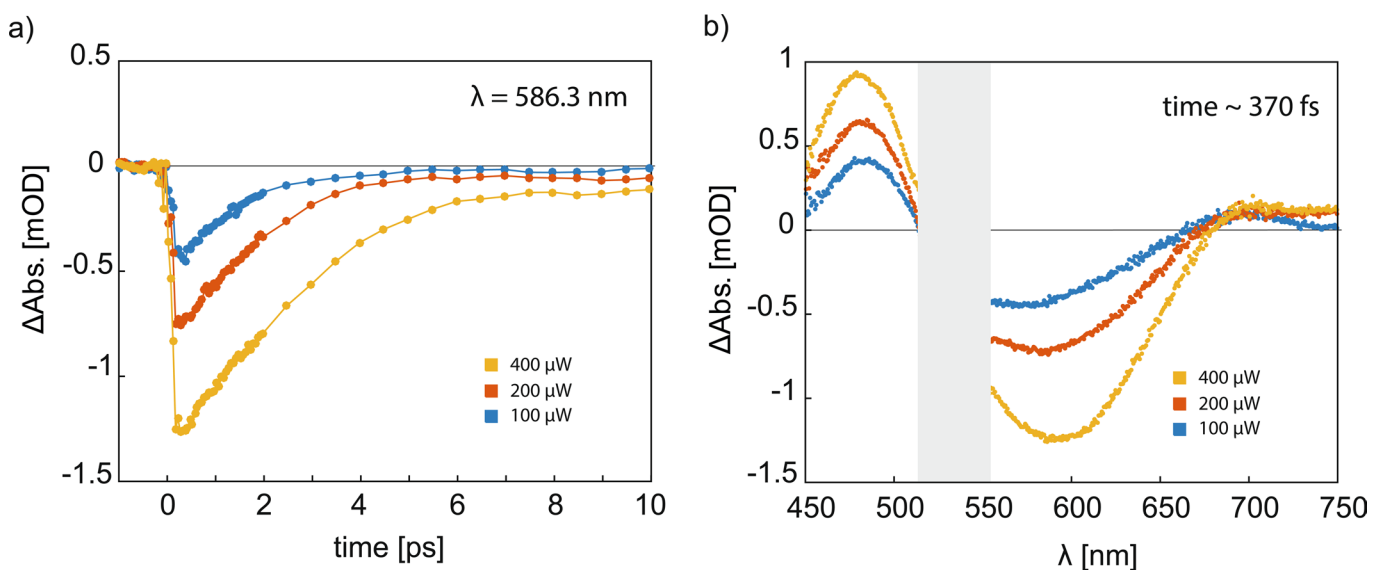
Extended Data Fig. 4 | Power-dependent pump-probe studies of visible-light transient absorption spectroscopy from Au/p-GaN heterostructures.

a, Power-dependent dynamics of the transient bleach at 560 nm from 200 μW to 500 μW pump power. **b**, Power-dependent differential transient absorption spectra ($\lambda_{\text{probe}} = 450 - 750 \text{ nm}$) from Au/p-GaN heterostructures cut at 350 fs.



Extended Data Fig. 5 | Power-dependent pump-probe studies of visible-light transient absorption spectroscopy from Au/Al₂O₃ heterostructures.

a, Power-dependent dynamics of the transient bleach at 550 nm from 100 μW to 400 μW pump power. **b**, Power-dependent differential transient absorption spectra ($\lambda_{\text{probe}} = 450 - 750 \text{ nm}$) from Au/p-GaN heterostructures cut at 350 fs.



Extended Data Fig. 6 | Power-dependent pump-probe studies of visible-light transient absorption spectroscopy from Au/SiO_2 heterostructures.

a, Power-dependent dynamics of the transient bleach at 586 nm from 100 μW to 400 μW pump power. **b**, Power-dependent differential transient absorption spectra ($\lambda_{\text{probe}} = 450 - 750 \text{ nm}$) from Au/SiO_2 heterostructures cut at 370 fs.